npj | flexible electronics

www.nature.com/npjflexelectron

ARTICLE OPEN

Check for updates

Squid-inspired and wirelessly controllable display for active camouflage in aquatic-environment

Doyoung Kim[1,6], Seung Won Seon[2,6], Minkyung Shin[3,4,6], Jihwan Kim[1], Bogeun Kim[1], Janghoon Joo[1], Sang Uk Park[1], Wooseok Kim[1], Hee Kyu Lee[1], Byeong Woon Lee[1], Se Gi Lee[1], Su Eon Lee[5], Ji-Hun Seo[4], Seung Ho Han[3]✉, Bong Hoon Kim[5]✉ and Sang Min Won[1]✉

Achieving optimal camouflage in an aquatic environment necessitates the ability to modulate transmittance in response to the surrounding obscurity and potential threats. This adaptation involves a dynamic transition from transparency to a deep-blue color, especially in low-light or dark situations. Such a strategy promotes a seamless assimilation with the surroundings, enabling the absorption of searchlights and, subsequently, diminishing the risk of detection by predators. Therefore, the presence of sophisticated mechanisms that facilitates stable and efficient control of transmittance is imperative, enabling smooth transition between transparent and deep-blue hues within the aquatic environment. This study presents nature-inspired programmable camouflage system that integrates an electrochromic display as the primary transmittance change element and a wireless base module for power and data transmission. Such technology offers a robust and flexible construction, ensuring stable operation as demonstrated through mechanical-fatigue experiments and quantitative simulation. A custom circuit and a power-control software package enable active control of multiple electrochromic displays while submerged in water.

npj Flexible Electronics (2024)8:7 ; https://doi.org/10.1038/s41528-024-00292-5

INTRODUCTION

Camouflage, a strategy to disguise an animal appearance, is defined as a morphological adaptation that blends an animal into its surroundings. Well-known camouflage methods include disruptive coloration (e.g., stripe pattern of zebra, spotted pattern of leopard, and military uniform) that utilizes a high-contrast pattern to obscure internal features and optical transparency (e.g., glass frog, jellyfish, and cephalopod) that reduces detectability by transmitting visible light without appreciable scattering. Species in terrestrial environments often employ the former strategy to conceal themselves in foliage and terrain. However, the range of color pigments, pattern resolution, and incapable adaptation to multiple environments represent key limitations[1–3]. The latter strategy involves optimal and intuitive mechanism for camouflage and is common in aquatic species[4] partly because of the difficulties in seeking creatures to blend in the open ocean, feasible similarity in refractive indexes between animal tissues and water, and unnecessary skin pigments to protect the organs from ultraviolet (UV) radiation[5]. In contrast, opaque coloration proves beneficial in dark environments as it effectively absorbs the searchlight emitted by predators, thereby minimizing both light scattering and visibility of the organism. An essential aspect of camouflage in an aquatic environment, thus, requires adjustable transmittance based on the turbidity and obscurity of the surroundings.

Recent research on the development of an active camouflage system relies on efforts in material engineering that adjusts the color and/or transparency through thermal[6,7], humidity[8], chemical[9,10], and electrical[11,12] triggers. The advantage of such active transformation allows adaptive camouflage depending on the surrounding environment. One specific example shows the electrically controlled chromic cells that can switch color from green (peak wavelength of 530 nm) to brown (peak wavelength of 640 nm) depending on the oxidation level of poly (2,7-carbazole)-derived materials[12]. Heterogeneous integration of thermochromic liquid-crystal polymer with a silver nanowire-based heater is another example that demonstrates artificial camouflage at the visible regime (wavelength from 400 to 700 nm)[6]. However, most of these actively triggered camouflagic materials utilize rigid and tethered control circuits with fragile mechanics, which are unsuitable for continuous communication and control in an aquatic environment. Inability to become transparent further limits ideal camouflaging. Another approach reveals programmable patterns through thermal switching of an ultrathin (thickness of ~10 μm) flexible-array network of leuco dyes[7], but binary-color change, tethered control system, and thermal-triggering mechanism remain incompatible with underwater camouflage.

The reef squid's camouflage tactic, wherein it alters its body transmittance in response to the surrounding environment, serves as an inspiration among various marine organisms, including octopuses and jellyfish (Fig. 1a). Here, the reef squid, known as *Sepioteuthis lessoniana*, achieves camouflage by controlling the size of chromatophores on its skin[13]. This mechanism allows the squid to modify its body transmittance, resulting in an increased resemblance to the surrounding backgrounds (Fig. 1b). Such modulation of transmittance serves to mitigate reflection from inanimate light sources such as diver's flashlights and the bioluminescence of potential predators

[1]Department of Electrical and Computer Engineering, Sungkyunkwan University, 2066, Seobu-ro, Jangan-gu, Suwon 16419, Republic of Korea. [2]Department of Smart Wearable Engineering, Soongsil University, Seoul 06978, Republic of Korea. [3]Electronic Convergence Materials and Devices Research Center, Korea Electronics Technology Institute (KETI), Seongnam 13509, Republic of Korea. [4]Department of Materials Science and Engineering, Korea University, Seoul 02841, Republic of Korea. [5]Department of Robotics and Mechatronics Engineering, DGIST, Daegu 42988, Republic of Korea. [6]These authors contributed equally: Doyoung Kim, Seung Won Seon, Minkyung Shin.
✉email: shhan@keti.re.kr; bonghoonkim@dgist.ac.kr; sangminwon@skku.edu

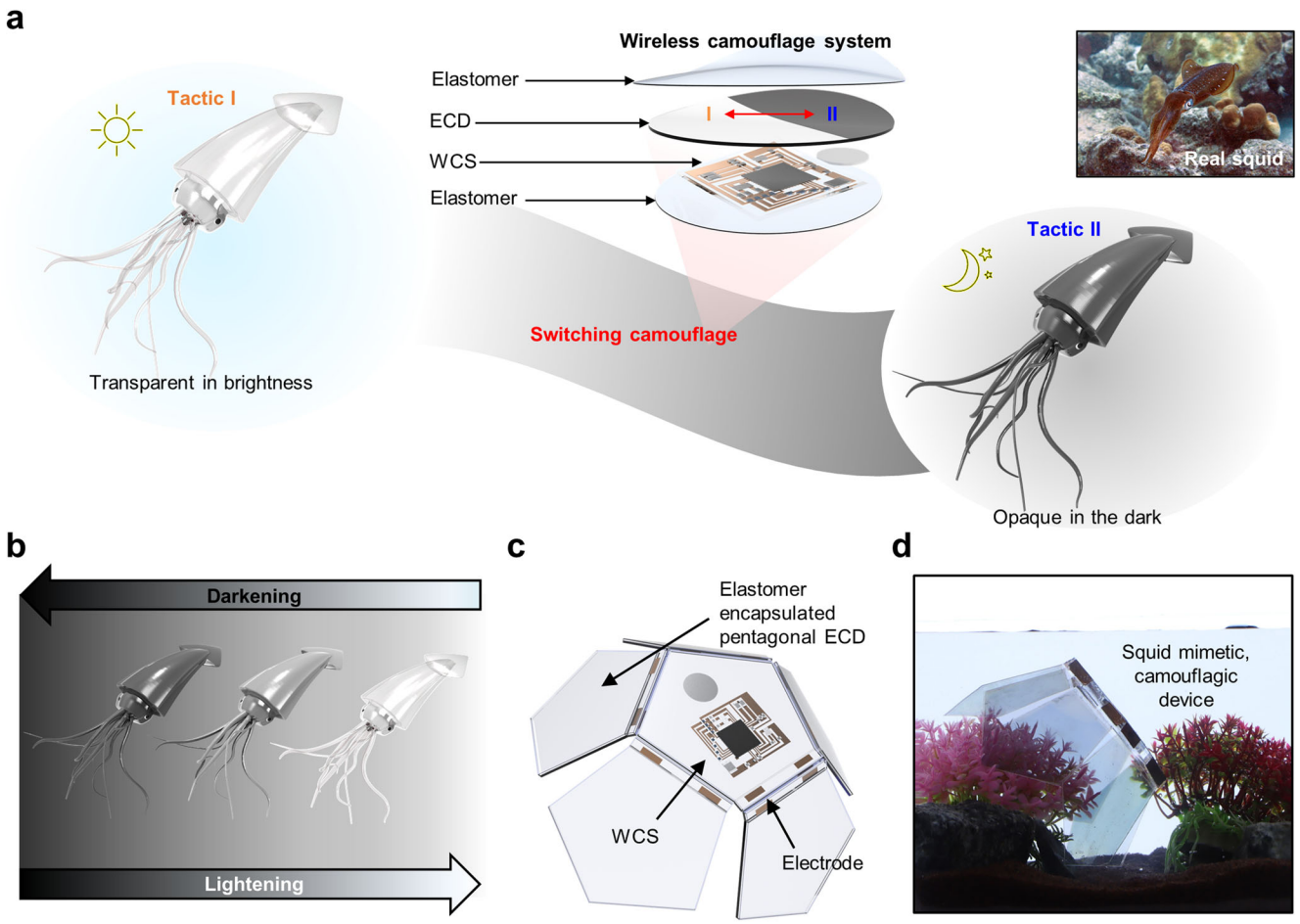

Fig. 1 Camouflage characteristics of the squid and the design of a biomimetic device that can change color according to the environment. a Conceptual illustration of the squid camouflage tactics (I and II) depending on the surrounding obscurity. The wireless camouflage system consists of ECDs and WCS that are encapsulated with elastomer. A real squid is shown in the inset. **b** Demonstration of body transmittance change mechanism according to the surrounding brightness. **c** Illustration of the squid-modeled device that consists of multiple ECDs and WCS. **d** Photograph of the camouflage device in the shallow aquatic environment. ECD electrochromic display, WCS wireless control system.

(Supplementary Fig. 1). This, in turn, significantly enhances the effectiveness of the camouflage.

The biomimetic camouflage device developed in this study replicates the dynamic transmittance modulation observed in squids by seamlessly integrating an electrochromic display (ECD) with a wireless control system (WCS), enabling effective camouflage in diverse environments (Fig. 1c, d). Electrically triggered redox reaction between tungsten trioxide (WO_3) and nickel oxide (NiO) via lithium (Li)-based polymeric electrolyte changes the ECD transmittance from being transparent to a deep-blue color (peak wavelength of 438 nm). Such optical property depends on the migration of Li ions within a multivalent transition metal–oxide layer similar to an electrochemical capacitor[14]. The device utilizes two different wireless protocols, i.e., near-field communication (NFC) and Bluetooth, for remote control of the optical transparency of the ECD. To enable seamless operation underwater, polydimethylsiloxane (PDMS) is employed as a water-resistant substrate and encapsulating elastomer[15]. The system flexibility is derived from ultrathin geometry (electrode and ECD thicknesses of 10 and 250 μm, respectively) and intrinsically flexible elastomer substrate. Consequently, the key features of a biomimetic active camouflage system designed for shallow water conditions include electrically adjustable transmittance, wireless control capability, water resistance, and flexibility. Notably, we have substantiated that the performance of these wireless devices exhibits minimal divergence in comparison to their wired counterparts.

RESULTS AND DISCUSSION

Structure of electrochromic display and its characteristics

Electrochromic coloration typically employs a multilayer configuration comprising distinct materials, including the counter electrode, ion-conducting electrolyte, and electrochromic layer. These components are all electrically linked through the use of two separate transparent conducting oxide. ECD in our study is composed of WO_3 and NiO, serving as the electrochromic layer and counter electrode, respectively. The fabrication procedure uses the concepts demonstrated for flexible ECD in which WO_3 and NiO are separately sputtered on top of an indium tin-oxide film and then assembled using a UV-curable Li-based polymeric electrolyte (Fig. 2a, b). Here, intercalation and deintercalation of the Li^+ ion due to an external direct voltage of 2.0 and −2.0, respectively, modulate the optical color of WO_3 from transparent to deep blue (peak wavelength of 438 nm) and/or vice versa. For example, transmittance of more than 70% at an applied voltage of 2.0 is reduced to 50%, 40%, and below 20% at external voltages of −1.0, −1.5, and −2.0, respectively, in the visible regime (Fig. 2c, d). The extensive range of colors

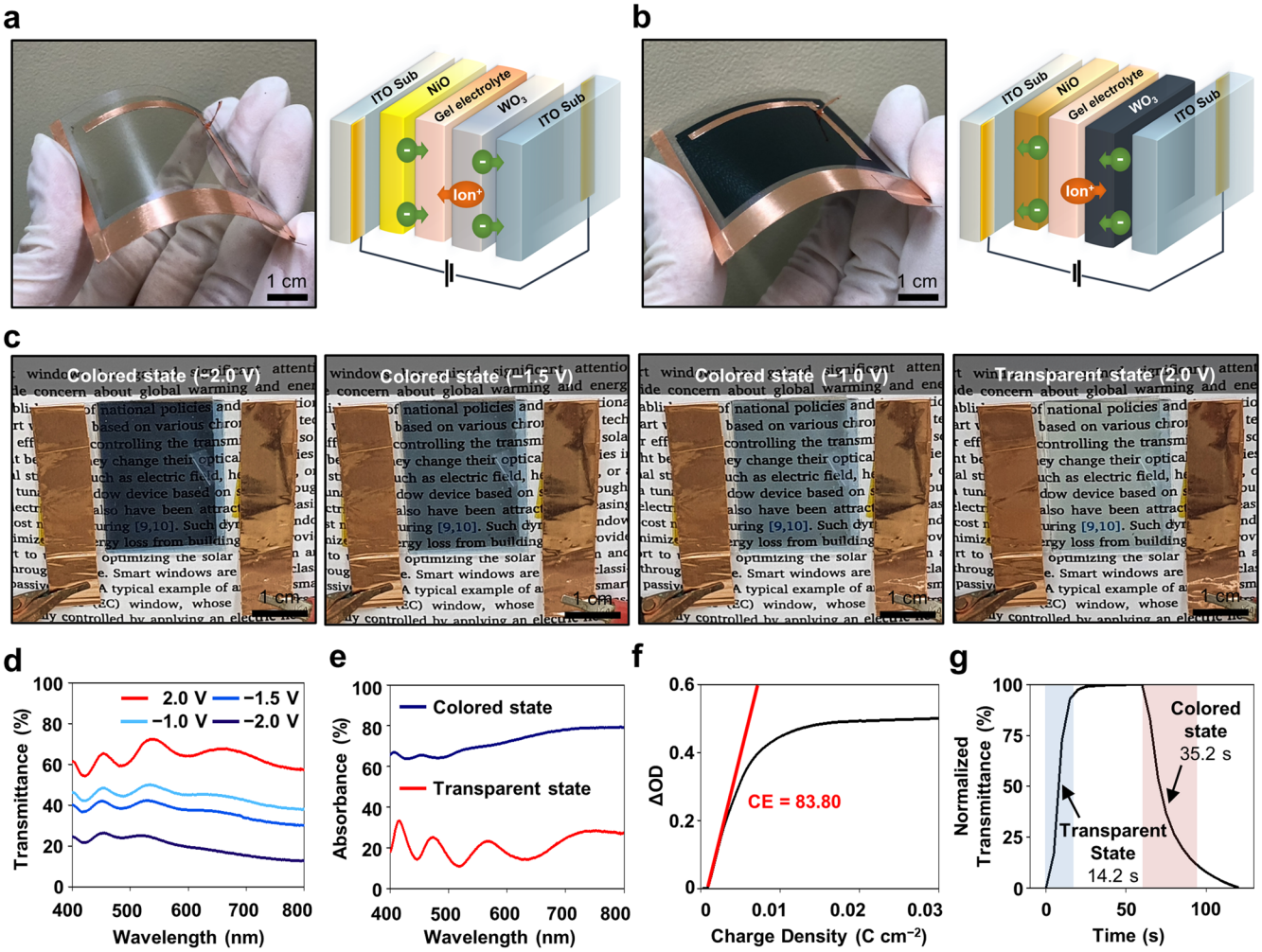

Fig. 2 Characterization of flexible ECD. Photographs and schematic of (**a**) transparent state and (**b**) colored state of ECD. **c** Photographs of the colored state with applied voltage of −2.0 V, −1.5 V, −1.0 V and transparent state (2.0 V) of ECD. **d** Optical transmittance spectra of the transparent (2.0 V) and colored states with external voltages of −1.0 V, −1.5 V, and −2.0 V. **e** Absorption spectra of the transparent and colored states of ECD. **f** Variation in the optical density relative to charge density measured at 550 nm. **g** Normalized transmittance during the pulse potential cycling. ECD electrochromic display.

exhibited by ECD can be quantified using red, green, and blue (RGB) values, which allows for the assessment of similarity between the ECD's color and the ambient color through the value of standard Euclidean similarity[16–19]. For instance, when the ECD is exposed to consistent light at 1.3 mW cm^{-2} from a light emitting diode (LED) light panel, it exhibits a similarity of 88.97%, nearly identical to the result presented in the manuscript. Such similarity value further increases by approximately 9% to 97.7% when the surrounding light intensity drops less than 0.2 μW cm^{-2} (Supplementary Fig. 2a). On the contrary, the colored state of the ECD exhibits significantly enhanced light absorbance, surpassing that of the transparent state by more than twofold (as shown in Fig. 2e and Supplementary Fig. 3). Results from additional evaluations conducted in diverse environments demonstrate that the similarities based on bending, tilted perspective, and salinity differences are comparable (Supplementary Fig. 4, 5a, and 2b). However, the similarity decreases by 9% (from 88 to 79%) when multiple ECDs overlap (Supplementary Fig. S5b), due to the light interference from the stacked multilayers.

Coloration efficiency (CE [cm^2 C^{-1}]) is a criterion used for comprehensive evaluation of electrochromic materials and represents the qualities of optical modulation with a given charge insertion or extraction. CE is expressed as

$$\mathrm{CE}(\lambda) = \frac{\Delta OD}{Q} \tag{1}$$

where Q is the charge inserted into or extracted from an electrochromic layer per unit area, and ΔOD denotes the change in the optical density, which is calculated as

$$\Delta \mathrm{OD} = \log\left(\frac{T_t(\lambda)}{T_c(\lambda)}\right). \tag{2}$$

The optical transmittance of the transparent (T_t, 71.4%) and colored (T_c, 22.5%) states at a wavelength of 550 nm results in ΔOD and CE values of 0.5 and 83.8 cm^2 C^{-1} (Fig. 2f), respectively, which are comparable with the values reported in similar systems[20–22]. The response time of the ECD is another crucial parameter for practical concern, and it can be determined by analyzing the 90% change in the normalized transmittance during a pulsed electrical-potential cycling test conducted between 2.0 and −2.0 Volts (Fig. 2g). The extracted values are 14.2 and 35.2 s for the bleaching and coloring processes, respectively, which are sufficiently fast for camouflage application in underwater

conditions[23,24]. Here, by making further modification to incorporate the intrinsic porous microstructure in both the cathodic and anodic electrochromic materials, in conjunction with the heightened ionic conductivity of the electrolyte, one can confer beneficial characteristics that have the potential to enhance the kinetics of ECD, resulting in an improved switching time compared to the current version[25–27]. Stable ECD performance can be demonstrated from electrical- and mechanical-fatigue experiments. The electrical pulse modulation, which causes a 35% transmittance change over 100 cycles, shows the stable property of ECD (Supplementary Fig. 6). Repetitive mechanical bending of flexible ECD (1000 cycles at a radius of 20.3 mm) results in slight degradation of the optical property in the visible regime partly due to the weakened adhesion at the electrolyte surfaces (Supplementary Fig. 7), which indicates that improved adhesion of electrolyte is an effective approach for improving mechanical stability. Conducting experiments to confirm the stability of our ECD, where it was submerged in a phosphate buffer solution at room temperature (pH 7.4) for 200 h, and exposed to a temperature of 60 °C in an oven-like environment, provides additional evidence of the device's operational stability (Supplementary Fig. 8).

Characteristics of flexible wireless control system with two different wireless protocols

Tether-based controls of ECD in aquatic environment not only limit the operating area in complex test arenas but also easily cause a relative wire motion due to the dynamic water flow, which can lead to electrical disconnection and inferior chronic stability. Therefore, developing a wireless control module is imperative for continuous operation in underwater locations. The wireless operating system consists of a flexible printed circuit board (thickness of 10 μm) embedded in a stretchable elastomer substrate and encapsulating material (i.e., PDMS) (Supplementary Fig. 9). The low modulus (1.32 MPa)[28] and inherent hydrophobic property of the encapsulating elastomer enable the system to operate in water, along with mechanical flexibility (Supplementary Fig. 10). Finite-element analysis of the wireless control module indicates that the maximum strain induced in the electrode at a bending radius of 6 mm is less than 0.54%, which is below the fracture limit (1%) (Supplementary Fig. 11). For example, cross-sectional images of an elastomer-encapsulated electrode using an optical microscope (Supplementary Fig. 12) reveal a stable interface between the copper film and the elastomer, irrespective of whether it is subjected to a flat configuration or a bending condition with a radius of 14.6 mm. The experimental result of the wireless-module operation soaked in phosphate buffered solution (pH 7.3, room temperature), as detailed in the Methods section, further confirms robust functionality in shallow underwater conditions (7 cm below the solution surface) with high output signal-to-noise ratio (126.98) and negligible latency (0.1 s) (Supplementary Fig. 13 and Supplementary Video 1).

The NFC technology, which relies on the inductive coupling between a primary transmitting coil and on-board secondary coil, can be a possible wireless control protocol in short-range underwater condition[29]. A relatively simple circuit design, as detailed in the method section, consists of two receiving coils, rectifiers, and multiplexer for power harvesting, analog-to-digital conversion, and output-sign conversion, respectively (Fig. 3a, b). Here, one receiving coil (RX coil 1) harvests power for the multiplexer inputs while another receiving coil (RX coil 2) provides the selectable bit (*b*), i.e., 1 or 0 bit, corresponding to the positive or negative voltages in the output node (V_1 and V_2) (Fig. 3c). In this circuitry, the output becomes negative when the wirelessly received power through RX coil 2 is insufficient (i.e., under 0.8 V) to provide selection bit of 1. (Fig. 3d and Supplementary Fig. 14). For example, the magnetic flux (φ), which diminishes in proportion to the antenna area (S) under the influence of the magnetic field ($\mathbf{B}$), is expressed as

$$\varphi = \int \mathbf{B} \cdot dS \tag{3}$$

The variation in magnetic flux over time leads to an induced output voltage in the RX coils, denoted as

$$V = -N\frac{d\varphi}{dt} \tag{4}$$

where N indicates the number of turns in the loop antenna. The regulation of power can be achieved by tilting or bending the RX coil, causing an angular misalignment between the transmitting coil and RX coil. Consequently, the output from the RX coil can be expressed as follows

$$V = \omega NS\mathbf{B}\cos\theta \tag{5}$$

where ω is the angular frequency, θ is the angle between the transmitting and receiving antennas. Since the system operates with the primary coil surrounding the test arena, when RX coil 2 is bent 0 ° to 60 °, it causes a reduction in voltage to a level below −7 dB compared to the initial value (2 V), leading to a change in polarity and the induction of a negative output affecting the color of the ECD. In contrast to RX coil 2, the voltage from RX coil 1 directly impacts the magnitude of the output from the NFC operating system in a similar manner. The results suggest the potential of automatic power control after additional integration of a functional material, such as shape-memory polymer, which can cause intentional tilting.

The board digital-signal processing and programmable operational control via Bluetooth low energy (BLE) protocol can further modulate multiple ECDs. Similar fabrication techniques, such as the use of NFC platform integrate the elastomer substrate and flexible electrode to support active (i.e., BLE microcontroller and antenna) and passive electronic components (i.e., capacitors and resistors) (Fig. 3e, f). Here, a low-energy dropout converter (LDO) reduces the output voltage to 2 Volts, making it suitable for ECD modulation (Fig. 3g). One possible output combination is to choose one output as a common node (i.e., V_d) and the other three as counterpart nodes (i.e., V_a, V_b, and V_c). The results shown in Fig. 3h illustrate the spontaneous change in the output from zero when the common node is the same as the counterpart nodes, either to positive or negative. These circuitry and program settings can be modified for applications that require modulation of a large number of ECDs. For example, a platform with four general-purpose inputs/outputs (GPIOs) in which each is wirelessly controlled through a tablet computer can supply separate positive and negative direct-current voltage to control a total of eight ECDs (Supplementary Fig. 15).

Integration of electrochromic display and wireless control system

Figure 4 shows wireless ECD in aquatic environments (pH 7.3, phosphate buffered solution). Figure 4a shows an image of a near-field wireless platform underneath ECD in transparent (top) and colored states (bottom). While the simplicity of the circuitry with NFC operation underwater offers advantages, the absence of a microcontroller makes it more practical to implement a limited number of controls for the ECD. The Bluetooth-controlled biomimetic squid with a pentagonal unit cell size of 21.1 cm^2 instead demonstrates scalability of the individual wireless control of ECD (Fig. 4b). In this case, the circuitry, which includes a battery underneath the single ECD unit cell, controls a total of six ECDs. The positive ECD electrodes are interconnected to six separate GPIOs, whereas the negative electrodes in all ECDs share a

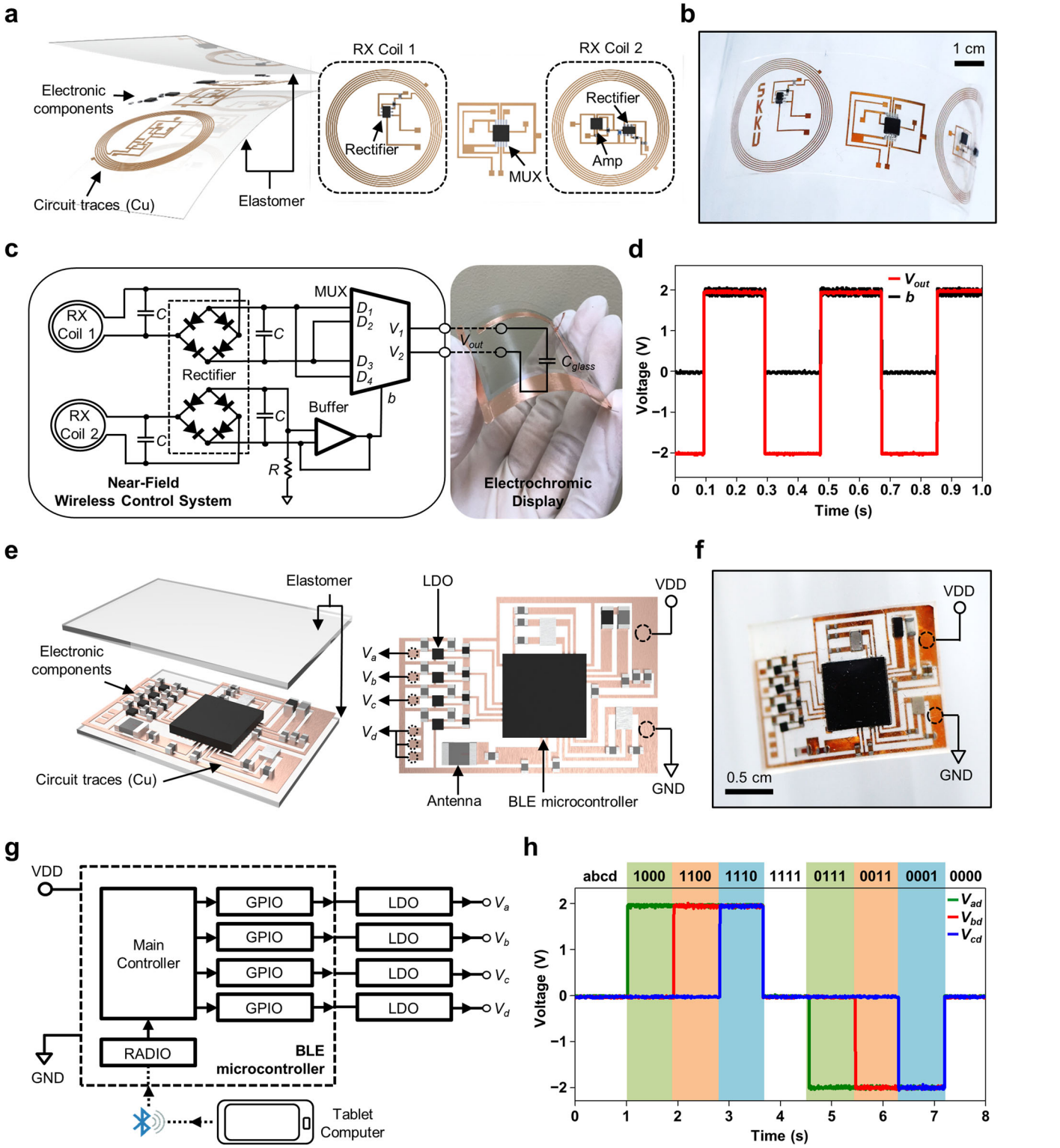

Fig. 3 Designs and output characteristics of flexible WCS. a Schematic illustration and exploded view of near-field WCS. **b** Photograph of near-field WCS. The system is attached to a substrate with a bending radius of 2.5 cm. **c** Circuitry of near-field WCS connected to ECD. **d** Output characteristic of near-field WCS, according to repetitive-signal-state changing of the multiplexer for 1 s. V_{out}: $V_1 - V_2$. **e** Schematic illustration and exploded-view of Bluetooth WCS. **f** Photograph of Bluetooth WCS. **g** Circuit and block diagram of Bluetooth WCS. A block diagram inside the BLE microcontroller is shown, and LDOs are connected to the microcontroller. This system can be wirelessly controlled by a tablet computer via BLE. **h** Combinational output characteristics (i.e., V_{ad}, V_{bd}, and V_{cd}) of Bluetooth WCS according to eight states from four GPIOs. RX receiving, MUX multiplexer, ECD electrochromic display, WCS wireless control system, GPIO general purpose input and output, LDO low dropout.

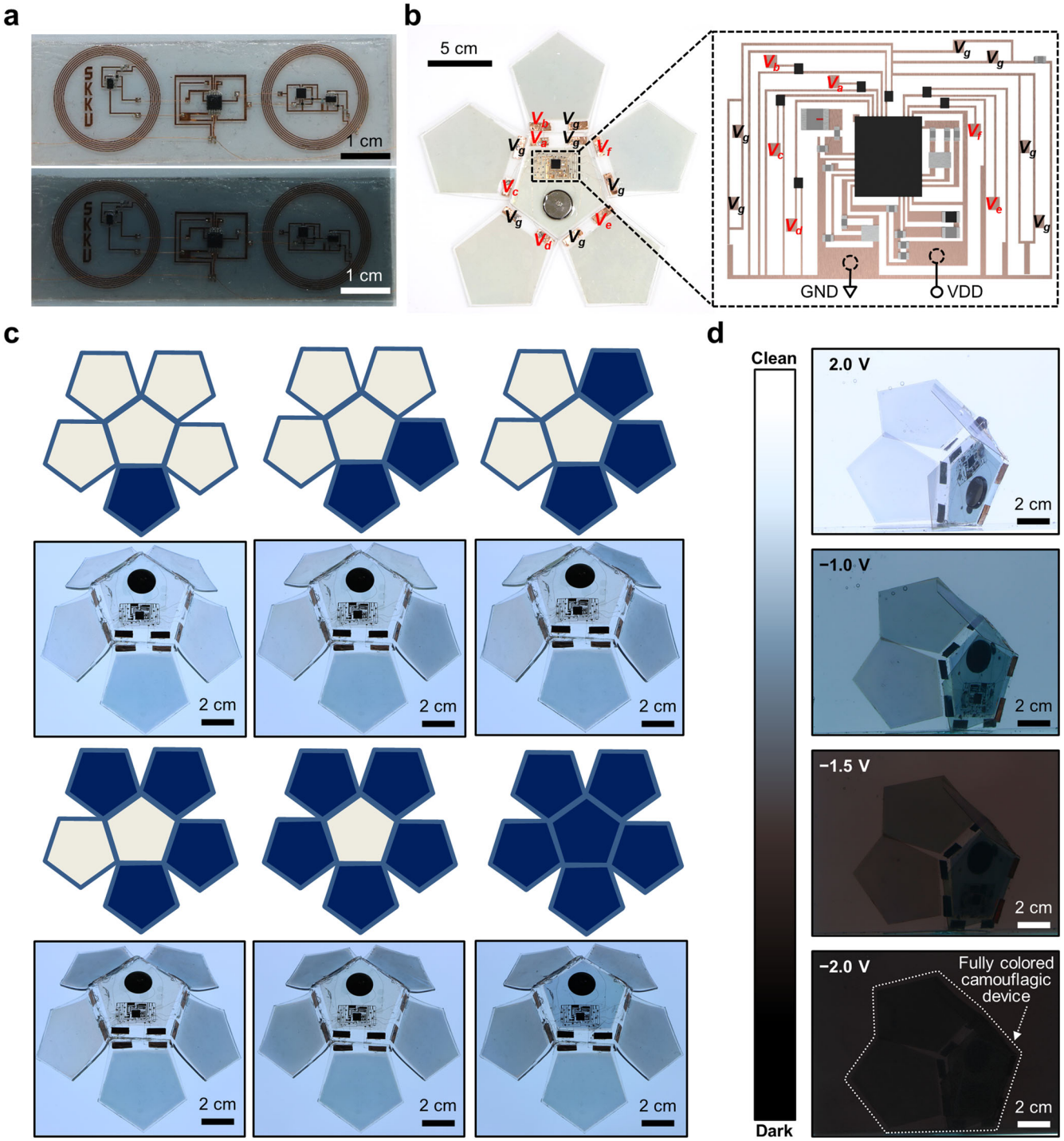

Fig. 4 Arrangement of wireless platforms and functional demonstrations on the camouflage effectiveness of the integrated device. **a** Photographs of ECD coloring operation by integrated near-field WCS. **b** Photograph and schematic of jellyfish mimetic device, which consist of six pentagonal ECDs and Bluetooth WCS. **c** Various camouflage patterns of a device with individually controlled ECDs by single WCS. **d** Demonstration of wirelessly adaptive camouflage depending on the water darkness. ECD electrochromic display, WCS wireless control system.

common GPIO node. The toggle switches in the tablet computer manipulate each GPIO pin, resulting in a dynamic camouflage pattern that can adapt to its surroundings (Fig. 4c). For example, Fig. 4d shows a camouflage strategy that uses different voltage sources and modulated transmittance of ECD according to the obscurity of the water. The application of various supplied voltages (ranging from 2.0 to −2.0 Volts) over time leads to different transmittances of the ECD. These varying transmittances make the ECD well-suited for creating effective camouflage conditions in gradually dimmed aquatic environments (Supplementary Video 2). The consistent electrical performance of the integrated system, which includes the ECD and wireless circuitry, following a 1000 cycle bending test, provides further validation of the system's durability (Supplementary Fig. 16). In this context, the

slight reduction in transmittance, as seen in previous bending tests involving single ECDs, can be partially attributed to weakened adhesion at the electrolyte surfaces. In the present study, a wireless ECD is demonstrated to operate in a shallow aquatic environment for a short duration, primarily due to the limited water-vapor-permeability rate of encapsulant[30,31]. However, it is worth noting that for long-term stability, bilayer encapsulation incorporating parylene and PDMS has been shown to be effective, as demonstrated in other researches[32–34], allowing the ECD to maintain stable performance over extended periods when exposed to aquatic conditions.

The results presented in this paper demonstrate a nature-inspired programmable wireless camouflage system that actively changes its transmittance from transparent to deep blue, resembling the behavior of aquatic species and effectively blending into the surrounding ocean environment. The comprehensive mechanical, electrical, and optical studies conducted on this system unveil its fundamental properties, including flexibility, stability, and transmittance. The integration of wireless circuitry, compatible with standard NFC and Bluetooth electronics, empowers programmable control of multiple ECDs, allowing dynamic camouflage patterns to be created while immersed in shallow water. This system and the set of demonstrations in this study present opportunities to use wireless controlled ECD as the basis for an advanced camouflagic system that is compatible with envisioned applications in military warships or diving suits. Incorporating additional sensing modules and functional materials into the system allows for enhanced automatic camouflage, responsive to environmental conditions, in addition to wireless user control. For example, one potential direction for future research involves integrating actuators, shape memory polymers, or mechanical motors into the substrate and encapsulation components to enable swimming capabilities[35–37]. While the user's operation range is currently constrained to shallow water areas due to limitations in underwater communication[38,39], the potential for deep-sea applications is promising[40] with advanced wireless protocols in the future.

METHODS

Fabrication of ECD

Indium tin-oxide-coated polyethylene terephthalate (ITO/PET) film (30 Ω sq^{-1}, Hansung Ind Co., Ltd) is used as substrate. The deposition of WO_3 and NiO are sputtered (CT-540, SUKWON) on separate substrates. Details of deposition conditions are described in our previous reports[41,42]. Two substrates (WO_3/ITO/PET and NiO/ITO/PET) are integrated with Li-based polymeric electrolyte (SWOPE, Soulbrain) that is cured using a UV crosslinker (UV LED Lab Dryer 150, Phoseion Technology). Such sputtering-based thin film process for ECD has the potential to achieve sub-micron scale resolution for each pixel, as demonstrated in prior research involving all-solid-state inorganic electrochromic display[42,43].

Transmittance, reflectance, and calculated absorbance of ECD

Optical transmittances of the transparent and colored states with external voltages of −1.0, −1.5, and −2.0 V of ECD (Fig. 2c) are measured in the wavelength range from 400 to 800 nm using a UV–visible (UV–VIS) spectrophotometer (clay-60, Agilent) (Fig. 2d). Continuous potential cycling of ECD is carried out for up to 100 cycles in the range from 2.0 to −2.0 V using the kinetic mode of the UV–VIS spectrophotometer at a wavelength of 550 nm (Supplementary Fig. 6). The transmittance (T) and reflectance (R) spectra of the transparent and colored states of ECD are measured using a UV–VIS–near-infrared spectrophotometer (V–670, JASCO) in the wavelength range from 400 to 800 nm (Supplementary Fig. 3). The absorbance (A) spectra (Fig. 2e) are obtained using the following equation:

$$A(\%) = 100 - T(\%) - R(\%). \quad (6)$$

Bending test of ECD and integrated device

A cycling bending test was conducted using a bending machine (ST-MO-XR1060-T-BENDING, SCIENCETOWN). The ECD component was subjected to a bending radius of 20.3 mm, while the integrated device was tested at a bending radius of 13.9 cm. These tests were performed at a constant speed of 1000 mm min^{-1} (Supplementary Fig. 7a and 16a). After bending cycles, the optical transmittance of the transparent and colored states of ECD with external voltages of 2.0 and −2.0 V, respectively, are measured using the scan mode of the UV–VIS spectrophotometer (clay-60, Agilent) in the wavelength range from 400 to 800 nm (Supplementary Fig. 7b and 16b).

Fabrication of WCS

Supplementary Fig. 9 shows a schematic cross-sectional illustration of the WCS fabrication. The substrate is made by spin coating (150 rpm, 60 s) PDMS (Sylgard 184, Dow) at a weight ratio of the base and curing agents of 10:1. A copper film (Cu, 10 μm) is attached to the PDMS substrate and patterned using an optical-fiber laser marker (HY-FMC20, HYOSUNG Laser). After the unnecessary copper-film parts are removed, electronic components and 34 AWG enamel-coated copper wires (Cu, Remington Industries) are soldered on the circuit trace. A top encapsulation layer is made by drop casting. After the encapsulation layer is cured (25 °C, 48 h), the entire device is peeled off from the glass to complete the fabrication.

Finite-element analysis of WCS

The strain distribution of the device under bending conditions is confirmed using commercial 3D finite-element analysis simulation program ABAQUS (ABAQUS/CAE, Ver. 6.24) (Supplementary Fig. 11). The hexahedronal elements (C3D20 in ABAQUS) consist of encapsulation layers (1 mm thick, PDMS), and the quadrilateral shell elements (S4 in ABAQUS) consist of circuit traces (10 μm thick, Cu). To bend the model, we use a rigid cylinder whose radius is equal to our target bending radius. We confirm the stability of the device under bending condition by comparing the maximum principal strain obtained from the simulation with the failure strain of copper (1%). The Young's modulus (E) and Poisson's ratio (v) are set as $E_{pdms} = 2660$ KPa and $v_{pdms} = 0.49$ for PDMS and $E_{copper} = 119$ GPa and $v_{copper} = 0.34$ for copper.

Circuitry of near-field WCS

Figure 3a, c show that the system can be divided into three parts: RX coil 1, RX coil 2, and multiplexer circuits. Both RX coils 1 and 2 are connected to a full-wave rectifier (BAS40XY,115, Nexperia) to obtain rectified direct-current power. From the RX coil 1 circuit, the positive node is connected to two inputs (i.e., D_1 and D_3) of the multiplexer (ADG787, Analog Devices), whereas the negative node is connected to another two inputs (i.e., D_2 and D_4). An operational amplifier (TSV991A, STmicroelectronics) is integrated into RX coil 2 to deliver signal to the selection node. The interconnections in the three parts are made using 34 AWG enamel-coated copper wires (Cu, Remington Industries).

Circuitry of bluetooth WCS

Figure 4b shows that six GPIO pins (i.e., V_a, V_b, V_c, V_d, V_e, and V_f) of the Bluetooth microcontroller (nRF52832, Nordic Semiconductor) are connected to the positive electrodes of six ECDs. A single GPIO pin (i.e., V_g) is connected to all the negative electrodes of six ECDs.

Seven LDOs (TCR2LN20, Toshiba) are used to decrease the output voltage of the seven GPIO pins. The connection from WCS to ECD uses 34 AWG enamel-coated copper wires (Cu, Remington Industries). The VDD and GND nodes are also connected to a coin-cell battery (CR2032, Toshiba) via the same copper wire.

Underwater feasibility test

In near-field WCS (Supplementary Fig. 10a), red (XZMER68W-3, SunLED) and green (XZVGR68W-3, SunLED) LEDs are connected in parallel to the output nodes with opposite polarity. The system is placed at the inner side of a 5 cm diameter vial, which contains 100 g of phosphate buffered solution (LB001-02, WELGENE). When only RX coil 1 is powered via TX coil 1, the red LED is turned on. When RX coil 2 is powered via TX coil 2 while RX coil 1 is powered, the polarity of the output in the multiplexer changes, which turns the red LED off and the green LED on. In Bluetooth WCS (Supplementary Fig. 10b), both the red and green LEDs are connected in series to the output circuit of the device. The device is immersed in a 7 cm diameter beaker that contains 50 g of phosphate buffered solution (LB001-02, WELGENE). The wireless connection between WCS and the tablet computer allows wireless toggling of the GPIO pin (Supplementary Fig. 17).

Near-field WCS output measurement

In the individual TX coil experiment (Fig. 3d and Supplementary Fig. 14), two TX coils with a diameter of 22.5 mm are separately connected to two waveform generators (3350B, KEYSIGHT) after setting a 13.56 MHz and 2.0 peak-to-peak voltage on TX coil 1 and a 13.56 MHz and 5.1 peak-to-peak voltage on TX coil 2 (Supplementary Fig. 18). The polarity changes are caused by the detachment of TX coil 2 from RX coil 2. The magnetic-field generating cage is made of $25 \times 25 \times 25$ cm^3 size with 1 mm thick acrylic sheet (Supplementary Fig. 10a). The magnetic field is generated by a power distribution controller (A6102-0198, NEUROLUX) through an antenna tuner (AUT-0150, NEUROLUX), which is connected to the wires around the cage. The power generator is set to 10 Hz current frequency, 100% period, and low-power mode. The angle between the bottom of the cage and the device is measured by a protractor (Supplementary Fig. 10c). The output values of all experiments are measured using a digital oscilloscope (DSOX1204A, KEYSIGHT) and a digital multimeter (Fluke 179, Fluke Corporation).

Wireless control of microcontroller via BLE

The wireless control of the microcontroller via the BLE interface iOS (iPad Air2 and iPhone8 Plus, Apple) application software uses the Swift language on the XCode development platform and Bluetooth microcontrol (nRF52832) system on chip (SoC) firmware, which controls the entire circuitry of the system. The software system as a whole is designed to control the voltage output of the SoC GPIOs connected to ECD proposed in this research. This functionality must be performed at precise timings determined by the user. Its action mechanism is described as follows. A connection between iOS and SoC must first be established. Then, the user can choose between the switches that are numbered from one to seven in the main view. Turning on these buttons immediately sends different string-based signals via Bluetooth to SoC, which are then parsed using a simple string-matching algorithm provided by the standard C library, triggering the voltage of the respective GPIO ports to HIGH or LOW. This process in turn determines the direction of the polarity of each display device. The nRF52 firmware code and its compatible iOS application code will be disclosed upon reasonable request.

Euclidean similarity

Each RGB values are extracted from the captured image of two subjects, ECD and background. The Euclidean distance (d) between the two subjects can be expressed as

$$d = \sqrt{(R_1 - R_2)^2 + (G_1 - G_2)^2 + (B_1 - B_2)^2} \tag{7}$$

where the RGB values of subject 1 and 2 express (R_1, G_1, B_1) and (R_2, G_2, B_2), respectively. Since the RGB values are natural numbers having a range from 0 to 255, the Euclidean similarity (s) can be represented based on the distance (d) between the two values as

$$s(\%) = \left(1 - \frac{d}{255\sqrt{3}}\right) \times 100 \tag{8}$$

Device operation testing according to the depth of water

To mimic the ionized properties of seawater, an aqueous solution is prepared by mixing Dulbecco's phosphate-buffered saline powder (D5652-50L, Sigma-Aldrich) with deionized water. This solution is then poured into a glass tank measuring $30 \times 30 \times 30$ cm^3. To ensure uniform distribution in all directions, a central stage is placed within the tank, as illustrated in Supplementary Fig. 13a. The Bluetooth Wireless Control System (WCS), featuring a red LED indicator of wireless disconnection, is vertically immersed above the stage. As the device is gradually lowered into the solution, the LED indicates the disconnection at a depth of 7 cm below the surface of the solution (Supplementary Fig. 13b and Supplementary Video 1).

Wireless power consumption

During Bluetooth wireless operation, the system exhibits a current consumption of 6 mA in advertising mode and 5.7 mA in connection mode (Supplementary Fig. 19a). When it comes to the camouflaging operation, an average of 11 mA is required for transitioning between colors (from transparent to colored, and vice versa) (Supplementary Fig. 19b). With this current consumption profile, the system, powered by a small-sized rechargeable coin cell battery with an 11 mAh capacity, can execute color changes for approximately 78 cycles and operate continuously for around 1.9 h without any color transitions. This system's operation can be enhanced by incorporating wireless battery charging functionality via the NFC antenna. This integration provides a stable 14 mA power supply to the rechargeable battery, as illustrated in Supplementary Fig. 19e, utilizing the primary coil surrounding the test arena. Under these conditions, the rechargeable coin cell battery (MS920SE, SEIKO) can be fully recharged in just 46 min, starting from a discharged state.

Wireless recharging device circuitry

The wireless charging circuit includes a full-wave rectifier (BAS40XY,115, Nexperia), a voltage regulator (LTC3255, Analog Devices), and passive components. These elements are interconnected with the frequency-matched inductive coil (Supplementary Fig. 19c, d).

Current consumption measurement

All current measurements include data related to power consumption during a single Electrochromic Display (ECD) transition, wireless communication, and recharging power. To acquire these measurements, we utilized a digital multimeter (NI USB-4065, National Instruments) (Supplementary Fig. 19a, b, e). The digital multimeter was connected to a personal computer (PC) and recorded real-time current values with a sampling rate of 0.2 milliseconds.

ECD durability test

Long-term durability test involves subjecting the ECDs, encapsulated in Polydimethylsiloxane (PDMS), to two different environmental conditions: immersion in water at room temperature and exposure to high-temperature conditions at 60 °C, each lasting for a duration of 200 hours. After the completion of the 200 hours test, we evaluated the optical properties of both the transparent and colored states of the ECDs. This assessment was carried out by applying external voltages of 2.0 V and −2.0 V and measuring optical characteristics within the wavelength range of 400 to 800 nm. The measurements were performed using the scan mode of a UV-VIS spectrophotometer (model clay-60, Agilent).

Bluetooth packet transfer performance analysis

Wireless communication software execution performance is considered by measuring the time taken for Bluetooth command being sent. The time includes UI execution time after user presses the GPIO turn-on button, Bluetooth packet formulation on physical layer and on-air time, and micro control unit (MCU) modem packet receive and internal microprocessor logic time. On the iOS side, precision timing using C-level API named mach_absolute_time() is utilized, whereas the microcontroller unit exploits nRF52 internal real time clock (RTC) timer. The RTC follows the specification as crystal oscillator frequency = 32.768 kHz and 1 tick = 30.52 µs. Here, an upper bound concept is used to explain that the specified operation always takes less than the maximum possible time. The results demonstrate that the entire process takes less than 0.1 s in both dry and underwater conditions.

Signal-to-noise ratio of output

The signal-to-noise ratio (SNR) of the output is defined as follows,

$$\mathrm{SNR} = \frac{\mu}{\sigma} \tag{9}$$

where μ and σ indicate the output mean and the standard deviation of output, respectively. The output values of the Bluetooth WCS are obtained using a digital oscilloscope (DSOX1204A, KEYSIGHT).

DATA AVAILABILITY

The data that support the findings of this study are either provided in the source data or are available from the corresponding author upon reasonable request.

Received: 12 August 2023; Accepted: 1 January 2024;
Published online: 05 March 2024

REFERENCES

1. Silberglied, R. E., Aiello, A. & Windsor, D. M. Disruptive coloration in butterflies: lack of support in Anartia fatima. *Science* **209**, 617–619 (1980).
2. Merilaita, S. Crypsis through disruptive coloration in an isopod. *Proc. R. Soc. Lond. Ser. B: Biol. Sci.* **265**, 1059–1064 (1998).
3. Jia, Q., Lv, X. L., Xu, W. D. & Hu, J. H. Intelligent design of gradual disruptive pattern painting and comparison of camouflage effectiveness. *Clust. Comput.* **22**, 9293–9301 (2019).
4. Johnsen, S. Hidden in plain sight: the ecology and physiology of organismal transparency. *Biol. Bull.* **201**, 301–318 (2001).
5. Johnsen, S. Hide and seek in the open sea: pelagic camouflage and visual countermeasures. *Annu. Rev. Mar. Sci.* **6**, 369–392 (2014).
6. Kim, H. et al. Biomimetic chameleon soft robot with artificial crypsis and disruptive coloration skin. *Nat. Commun.* **12**, 4658 (2021).
7. Yu, C. et al. Adaptive optoelectronic camouflage systems with designs inspired by cephalopod skins. *Proc. Natl. Acad. Sci. U.S.A.* **111**, 12998–13003 (2014).
8. Gao, W. et al. Reversible luminescent humidity chromism of organic–inorganic hybrid PEA 2 MnBr 4 single crystals. *Dalton Trans.* **49**, 5662–5668 (2020).
9. Reichardt, C. Solvatochromic dyes as solvent polarity indicators. *Chem. Rev.* **94**, 2319–2358 (1994).
10. Favaro, G., Clementi, C., Romani, A. & Vickackaite, V. Acidichromism and ionochromism of luteolin and apigenin, the main components of the naturally occurring yellow weld: a spectrophotometric and fluorimetric study. *J. Fluorescence* **17**, 707–714 (2007).
11. Cai, G. et al. Multicolor electrochromic film based on TiO_2@ polyaniline core/shell nanorod array. *J. Phys. Chem. C.* **117**, 15967–15975 (2013).
12. Beaupré, S., Breton, A.-C., Dumas, J. & Leclerc, M. Multicolored electrochromic cells based on poly (2, 7-carbazole) derivatives for adaptive camouflage. *Chem. Mater.* **21**, 1504–1513 (2009).
13. Nakajima, R. et al. Squid adjust their body color according to substrate. *Sci. Rep.* **12**, 5227 (2022).
14. Simon, P. & Gogotsi, Y. Materials for electrochemical capacitors. *Nat. Mater.* **7**, 845–854 (2008).
15. Jin, M. et al. Super-hydrophobic PDMS surface with ultra-low adhesive force. *Macromol. Rapid Commun.* **26**, 1805–1809 (2005).
16. Woo, T. et al. The dynamics of pattern matching in camouflaging cuttlefish. *Nature* **619**, 122–128 (2023).
17. Zhou, X., Zhu, W., Liu, F., Yang, W. & Chu, M. in *2022 7th International Conference on Communication, Image and Signal Processing (CCISP)*. 178–182 (IEEE).
18. Zhang, B., Zheng, W., Zhou, J. & Lu, J. in *Proceedings of the IEEE/CVF Conference on Computer Vision and Pattern Recognition*. 7532–7541.
19. Wang, Z. Image quality assessment: form error visibility to structural similarity. *IEEE Trans. Image Process.* **13**, 604–606 (2004).
20. Yun, T. Y., Li, X., Bae, J., Kim, S. H. & Moon, H. C. Non-volatile, Li-doped ion gel electrolytes for flexible WO_3-based electrochromic devices. *Mater. Des.* **162**, 45–51 (2019).
21. Liu, Y. et al. Preparation of WO3 gel electrochromic device by simple two-step method. *Mater. Today Commun.* **30**, 103090 (2022).
22. Chen, W. et al. A novel ionically crosslinked gel polymer electrolyte as an ion transport layer for high-performance electrochromic devices. *J. Mater. Chem. C.* **7**, 3744–3750 (2019).
23. Song, X. et al. Properties of NiOx and its influence upon all-thin-film ITO/NiOx/$LiTaO_3$/WO_3/ITO electrochromic devices prepared by magnetron sputtering. *Vacuum* **111**, 48–54 (2015).
24. Liu, Q. et al. An all-thin-film inorganic electrochromic device monolithically fabricated on flexible PET/ITO substrate by magnetron sputtering. *Mater. Lett.* **142**, 232–234 (2015).
25. Rai, V., Singh, R. S., Blackwood, D. J. & Zhili, D. A review on recent advances in electrochromic devices: a material approach. *Adv. Eng. Mater.* **22**, 2000082 (2020).
26. Marcilla, R. et al. Tailor-made polymer electrolytes based upon ionic liquids and their application in all-plastic electrochromic devices. *Electrochem. Commun.* **8**, 482–488 (2006).
27. Yang, G. et al. Advances in nanomaterials for electrochromic devices. *Chem. Soc. Rev.* **49**, 8687–8720 (2020).
28. Johnston, I. D., McCluskey, D. K., Tan, C. K. & Tracey, M. C. Mechanical characterization of bulk Sylgard 184 for microfluidics and microengineering. *J. Micromech. Microeng.* **24**, 035017 (2014).
29. Pozzebon, A. in *2015 International EURASIP Workshop on RFID Technology (EURFID)*. 152–156 (IEEE).
30. Robb, W. Thin silicone membranes-their permeation properties and some applications. *Ann. NY: Acad. Sci.* **146**, 119–137 (1968).
31. Bian, P., Wang, Y. & McCarthy, T. J. Rediscovering Silicones: the anomalous water permeability of "hydrophobic" PDMS suggests nanostructure and applications in water purification and anti-icing. *Macromol. Rapid Commun.* **42**, 2000682 (2021).
32. Shin, G. et al. Flexible near-field wireless optoelectronics as subdermal implants for broad applications in optogenetics. *Neuron* **93**, 509–521.e503 (2017).
33. Mickle, A. D. et al. A wireless closed-loop system for optogenetic peripheral neuromodulation. *Nature* **565**, 361–365 (2019).
34. Ausra, J. et al. Wireless, battery-free, subdermally implantable platforms for transcranial and long-range optogenetics in freely moving animals. *Proc. Natl Acad. Sci.* **118**, e2025775118 (2021).
35. Wang, T. et al. A versatile jellyfish-like robotic platform for effective underwater propulsion and manipulation. *Sci. Adv.* **9**, eadg0292 (2023).
36. Wang, Y., Zhang, P., Huang, H. & Zhu, J. Bio-inspired transparent soft jellyfish robot. *Soft Robot.* **10**, 590–600 (2023).
37. Matharu, P. S. et al. Jelly-Z: swimming performance and analysis of twisted and coiled polymer (TCP) actuated jellyfish soft robot. *Sci. Rep.* **13**, 11086 (2023).
38. Lloret, J., Sendra, S., Ardid, M. & Rodrigues, J. J. Underwater wireless sensor communications in the 2.4 GHz ISM frequency band. *Sensors* **12**, 4237–4264 (2012).
39. Tahir, M., Yan, P. & Shuo, L. Channel characterization of EM waves propagation at MHz frequency through seawater. *Int. J. Commun. Syst.* **31**, e3462 (2018).
40. Kebkal, K., Mashoshin, A. & Morozs, N. Solutions for underwater communication and positioning network development. *Gyroscopy Navig.* **10**, 161–179 (2019).

41. Lee, S. J. et al. Investigation of all-solid-state electrochromic devices with durability enhanced tungsten-doped nickel oxide as a counter electrode. *J. Alloy. Compd.* **815**, 152399 (2020).
42. Lee, S. H. et al. Durability-enhanced monolithic inorganic electrochromic devices with tantalum-doped nickel oxide as a counter electrode. *Sol. Energy Mater. Sol. Cells* **234**, 111435 (2022).
43. Lee, S. J. et al. VO_2/WO_3-based hybrid smart windows with thermochromic and electrochromic properties. *ACS Sustain. Chem. Eng.* **7**, 7111–7117 (2019).

ACKNOWLEDGEMENTS

S.M.W. acknowledges support by a National Research Foundation of Korea (NRF) grant funded by the Korea government (MSIP; Ministry of Science, ICT & Future Planning; grant no. NRF-2021R1C1C1009410, NRF-2022R1A4A3032913 and IITP-2020-0-01821). S.M.W. acknowledges the support by Nano Material Technology Development Program (2020M3H4A1A03084600) through the National Research Foundation of Korea (NRF) funded by the Ministry of Science and ICT of Korea. B.H.K. acknowledges the support by the National Research Foundation of Korea (NRF) grant funded by the Korea government (MSIT) (No.2022M3H4A1A02046445).

COMPETING INTERESTS

The authors declare no competing interests.

ADDITIONAL INFORMATION

Supplementary information The online version contains supplementary material available at https://doi.org/10.1038/s41528-024-00292-5.

Correspondence and requests for materials should be addressed to Seung Ho Han, Bong Hoon Kim or Sang Min Won.